JOURNAL OF THE AMERICAN CHEMICAL SOCIETY

Article

Lattice Hydride Mechanism in Electrocatalytic CO2 Reduction by Structurally Precise Copper-Hydride Nanoclusters

Qing Tang, Yongjin Lee, Dai-Ying Li, Woojun Choi, C.W. Liu, Dongil Lee, and De-en Jiang

J. Am. Chem. Soc., **Just Accepted Manuscript** • Publication Date (Web): 22 Jun 2017

Just Accepted

ACS Publications

Journal of the American Chemical Society is published by the American Chemical Society. 1155 Sixteenth Street N.W., Washington, DC 20036

Lattice Hydride Mechanism in Electrocatalytic CO_2 Reduction by Structurally Precise Copper-Hydride Nanoclusters

Qing Tang,[†] Yongjin Lee,[‡] Dai-Ying Li,[§] Woojun Choi,[‡] C. W. Liu,*[,§] Dongil Lee,*[,‡] and De-en Jiang*[,†]

[†]Department of Chemistry, University of California, Riverside, CA 92521, USA

[‡]Department of Chemistry, Yonsei University, Seoul 03722, South Korea

[§]Department of Chemistry, National Dong Hwa University, Hualien 97401, Taiwan, R.O.C.

*To whom correspondence should be addressed. E-mail: chenwei@mail.ndhu.edu.tw, dongil@yonsei.ac.kr, djiang@ucr.edu.

ABSTRACT: Copper electrocatalysts can reduce CO_2 to hydrocarbons at high overpotentials. However, mechanistic understanding of CO_2 reduction on nanostructured Cu catalysts has been lacking. Herein we show that the structurally precise ligand-protected Cu-hydride nanoclusters, such as $Cu_{32}H_{20}L_{12}$ (L is a dithiophosphate ligand), offer unique selectivity for electrocatalytic CO_2 reduction at low overpotentials. Our density functional theory (DFT) calculations predict that the presence of the negatively charged hydrides in the copper cluster plays a critical role in determining the selectivity of the reduction product, yielding HCOOH over CO with a lower overpotential. The HCOOH formation proceeds via the lattice hydride mechanism: first, surface hydrides reduce CO_2 to HCOOH product, and then the hydride vacancies are readily regenerated by the electrochemical proton reduction. DFT calculations further predict that hydrogen evolution is less competitive that HCOOH formation at the low overpotential. Confirming the predictions, electrochemical tests of CO_2 reduction on the $Cu_{32}H_{20}L_{12}$ cluster demonstrate that HCOOH is indeed the main product at low overpotential while H_2 production dominates at higher overpotential. The unique selectivity afforded by the lattice-hydride mechanism opens the door for further fundamental and applied studies of electrocatalytic CO_2 reduction by copper-hydride nanoclusters and other metal nanoclusters that contain hydrides.

1. INTRODUCTION

The increasing emission of CO_2 into atmosphere due to the burning of fossil fuels and other human activities has been shown to be the main contributor to global warming and climate change.[1,2] A promising strategy to alleviate this concern is to convert CO_2 into useful fuels and chemicals.[3,4] CO_2 itself is, however, very stable and relatively inert, making its chemical conversion challenging due to the need of large energy input and efficient catalysts. Among the different methods developed for CO_2 reduction, electrochemical reduction has attracted great attention since it is undertaken at ambient conditions and can be powered by renewable energy.[5,6]

Numerous research efforts have focused on transition-metal electrocatalysts;[7] in particular, copper has stood out due to its unique ability to produce significant amounts of hydrocarbons from CO_2 electroreduction. The product distribution is found to be potential-dependent on Cu:[8-13] at a less negative potential or small overpotential, formation of H_2, HCOOH and CO is predominant, while at a sufficiently higher overpotential, formation of CH_4 and C_2H_4 becomes major. A main drawback for CO_2 electroreduction on the Cu surface is that the hydrocarbon formation takes place only at a high overpotential of about 1 eV.

Understanding how CO_2 is reduced on the Cu surface can shed light on the design of new catalysts that decrease the onset overpotential and increase the product selectivity. As such, many recent experimental[14-25] and theoretical[26-32] studies have examined the catalytic mechanism of CO_2 reduction on the metallic copper surface. It is generally accepted that CO is the key intermediate to formation of CH_4 and C_2H_4. Although the high-quality single-crystal Cu surfaces can serve as useful benchmark models to elucidate how Cu catalyzes the electroreduction of CO_2, these model systems usually have low specific surface areas. Instead, Cu nanoparticles have been recently explored to tune the electrocatalytic activity; the morphology and particle size of the copper crystals/nanoparticles have been shown to have a dramatic influence on the catalytic activity and product selectivity of CO_2 electroreduction.[33-35]

Although nanostructured Cu catalysts have been widely investigated for the electroreduction of CO_2, their surface structures are not well defined to serve as a model to reveal the mechanism of CO_2 reduction. Different from the bulk metal surfaces and

larger nanoparticles, ligand-protected atomically precise metal clusters exhibit not only well-defined atomic structures, but also size-dependent electronic, chemical and catalytic properties. Many atomically precise Au[36,37] and Ag[38-41] clusters have been synthesized recently, with thiolate,[42-44] phosphine,[45] or alkynyl ligands.[46-49] More excitingly, several ligand-protected copper-hydride nanoclusters,[50] such as $[Cu_{14}H_{12}(phen)_6(PPh_3)_4][X]_2$,[51] $[Cu_{18}H_7\{1,2\text{-}S(C_6H_4)PPh_2\}_{10}(I)]$,[52] $[Cu_{20}H_{11}\{S_2P(O^iPr)_2\}_9]$,[53,54] $[Cu_{25}H_{22}(PPh_3)_{12}]Cl$,[55] $[Cu_{28}H_{15}(S_2CNR)_{12}]PF_6$,[56] and $Cu_{32}H_{20}\{S_2P(O^iPr)_2\}_{12}$,[57] have been crystallized. A particularly interesting feature in these copper clusters is the presence of hydrides (H^-) which can be found at the capping (or surface) sites and/or the interstitial sites. These atomically and structurally precise Cu clusters with their well-defined structures provide a unique opportunity to understand the mechanism of electrocatalytic CO_2 reduction and to reveal the role of the hydride ligands that could lead to new mechanistic insights and product selectivity. To the best of our knowledge, these structurally precise Cu-H clusters have not been tested for electrochemical CO_2 reduction.

Among the experimentally realized, structurally precise Cu-H clusters, the neutral $Cu_{32}H_{20}L_{12}$ cluster (L= $S_2P(O^iPr)_2$) offers a diverse set of hydrides of different coordination environments that could offer synergy in CO_2 reduction. In this work, we use the $Cu_{32}H_{20}L_{12}$ cluster as the prototypical Cu-H nanosystem to investigate its activity and selectivity for electrochemical reduction of CO_2: first, we reveal the role of hydrides and predict the product selectivity by density functional theory (DFT) calculations; then. we test the electrocatalytic activity of the synthesized $Cu_{32}H_{20}L_{12}$ cluster in an aqueous solution.

2. METHODS

Computational. Spin-polarized DFT calculations were performed to investigate the electrocatalytic activity of $Cu_{32}H_{20}L_{12}$ nanocluster for CO_2 reduction by using the Vienna *ab initio* simulation package (VASP).[58] To save the computational cost, we simplified L from $S_2P(O^iPr)_2$ to S_2PH_2 as done by others.[54,57] The ion-electron interaction is described with the projector augmented wave (PAW) method.[59] Electron exchange-correlation is represented by the functional of Perdew, Burke and Ernzerhof (PBE) of generalized gradient approximation (GGA).[60] A cutoff energy of 400 eV was used for the plane-wave

basis set. The van der Waals interactions were considered and described using the empirical correction in Grimme's scheme (DFT-D3).[61] The $Cu_{32}H_{20}L_{12}$ nanocluster was placed in a cubic box with dimension of 25×25×25 Å^3. The rod-like cluster is about 1.2 nm in diameter (in the *xy* plane) and 1.35 nm in length (along the *z* direction), and the vacuum space distance along the x, y and z directions is 12 Å, 11 Å, and 14 Å, respectively. Only the Γ-point was used to sample the Brillouin zone. The climbing-image nudged elastic band (CI-NEB) method[62] implemented in VASP was used to determine the minimum energy paths for the non-electrochemical elementary step. The convergence threshold for structural optimization was set to be 10^{-4} eV in energy and 0.03 eV/Å in force. The transition states were obtained by relaxing the force below 0.05 eV/Å.

The reaction free energies of the electrochemical steps with the involvement of proton-electron pair were calculated using the computational hydrogen electrode proposed by Nørskov et al.[63] The change in Gibbs free energy (ΔG) for all the electrochemical or non-electrochemical steps was defined as $\Delta G = \Delta E + \Delta E_{zpe} - T\Delta S$, where ΔE is the different in the DFT total energy, ΔE_{zpe} is the zero-point energy difference calculated from the vibrational frequencies, and ΔS is the entropy difference between the products and the reactants. The entropies of the free molecules at 298K and 1 atm were taken from the NIST database, while the vibrational entropy was considered for the adsorbed species. In this work, we considered the reduction of CO_2 to HCOOH and CO products. To improve the accuracy of PBE functional in predicting the free energy of reaction species, we considered the following three types of correction: DFT energy correction of free CO_2 and CO molecules; the solvation effect of COOH*, OH* and CO* species; liquid-phase correction of H_2O and HCOOH products. Details of the corrections are provided in Supporting Information, including Tables S1 and S2.

Synthesis of $[Cu_{32}(H)_{20}\{S_2P(O^iPr)_2\}_{12}]$. The Cu_{32} cluster was prepared via the previously reported method[57] and details are provided in Supporting Information. Briefly, $[Cu(CH_3CN)_4](PF_6)$ (0.500 g, 1.340 mmol) dissolved in 10 mL CH_3CN was transferred to the cooled mixture of $NH_4[S_2P(O^iPr_2)_2]$ and $[NaBH_4]$ suspended in 30 mL CH_3CN. After stirring at 10 ^oC for 4 h, 0.2 mL of MeOH was added to reaction mixture over 1 h, and then the solvent was evaporated under vacuum. The residue was dissolved in 20 mL

dichloromethane (DCM) and washed with deionized water (2 × 30 mL). After the filtrate from the DCM layer was evaporated under vacuum, 30 mL methanol was added to the dry residue, leading to a turbid solution that was placed in a freezer for several hours for the precipitate to settle down. The obtained brown precipitate was further washed with acetone and then dried under vacuum, yielding a brown precipitate of $[Cu_{32}(H)_{20}\{S_2P(O^iPr)_2\}_{12}]$ (0.079 g, 41%, based on Cu), which was confirmed by melting point, elemental analysis, ESI-MS, ^{1}H-NMR, and ^{31}P-NMR.

Electrocatalysis experiments. Controlled potential electrolysis (CPE) experiments were carried out for 90 min under vigorous stirring with a ZIVE MP1 potentiostat (WonATech, Korea) in an H-type cell that was equipped with a composite working electrode, and a Ag/AgCl (3 M NaCl) reference electrode in one compartment and a platinum plate (1.68 cm^2) counter electrode in the other compartment. The working electrode and the counter electrode were separated by a proton-exchange membrane (Nafion 117; Sigma-Aldrich). Both compartments were filled with 60 mL of 0.1 M $KHCO_3$ and 0.4 M KCl solution. The working electrode compartment was saturated with CO_2 gas. The composite working electrode was fabricated by spreading a catalyst ink, prepared by mixing 80 μg of the $Cu_{32}(H)_{20}\{S_2P(O^iPr)_2\}_{12}$ cluster catalyst, 200 μg of carbon black (Vulcan XC-72) and 3.5 μL of Nafion solution (5 wt%, Sigma-Aldrich) in 50 μL of tetrahydrofuran, on a gas diffusion layer (GDL, model N1S1007, CeTech Co., Taiwan) electrode (2 cm^2). The amounts of CO and H_2 produced were quantified from an analysis of the headspace using an Agilent 7890B gas chromatography equipped with a flame ionization detector and thermal conductivity detector. HCOOH production was quantified by calibrating the ^{1}H NMR spectrum (Bruker Avance II 400 MHz NMR spectrometer) of the product solution against 100 ppm acetic acid used as an internal standard.

3. RESULTS AND DISCUSSION

3.1. Hydrides in the $Cu_{32}H_{20}L_{12}$ nanocluster. Figure 1 shows the optimized structure of $Cu_{32}H_{20}L_{12}$ nanocluster. The Cu_{32} skeleton can be viewed as a distorted hexacapped rhombohedral core of 14 Cu atoms sandwiched between two nest-like triangular cupola fragments of Cu atoms (each cupola comprises of 9 Cu atoms). The 20 hydrides can be grouped into 12 tri-coordinated H (μ_3-H, capping mode), six tetra-coordinated H (μ_4-H,

interstitial mode), and two penta-coordinated H (μ_5-H, interstitial mode). The 12 μ_3-H hydrides can be further divided into three μ_3-H1, two μ_3-H2, four μ_3-H3, and two μ_3-H4. Both μ_3-H1 and μ_3-H2 are coordinated to the Cu_3 triangle of the periphery cupola fragments: μ_3-H1 neighbors to μ_4-H1 and μ_4-H2, while μ_3-H2 neighbors to μ_4-H2 and μ_5-H (as clearly seen in Figure 1). Both μ_3-H3 and μ_3-H4 (at the central part) bridge Cu_3 triangles of the hexacapped rhombohedron: the difference is that one of μ_3-H3's three coordinated Cu atoms is a central Cu without any bonding to S. The six μ_4-H hydrides can be divided into four μ_4-H1 and two μ_4-H2: μ_4-H1 is located in a tetrahedral interstitial site at the interface between the central hexacapped rhombohedron and the periphery cupola, while μ_4-H2 is located at a tetrahedral interstitial site of the periphery cupola. The calculated Bader charges (Table 1) show that these hydrides have a negative charge of -0.25 ~ -0.34|e|, while the Cu atoms bonded directly with the hydrides and/or the L ligands carry a positive charge (+0.20 ~ +0.45 |e|). The many lattice hydrides in the Cu clusters can provide the hydrogen source needed for CO_2 reduction, against the commonly assumed proton-reduction channel whereby hydrogen is sourced from the proton in solution.

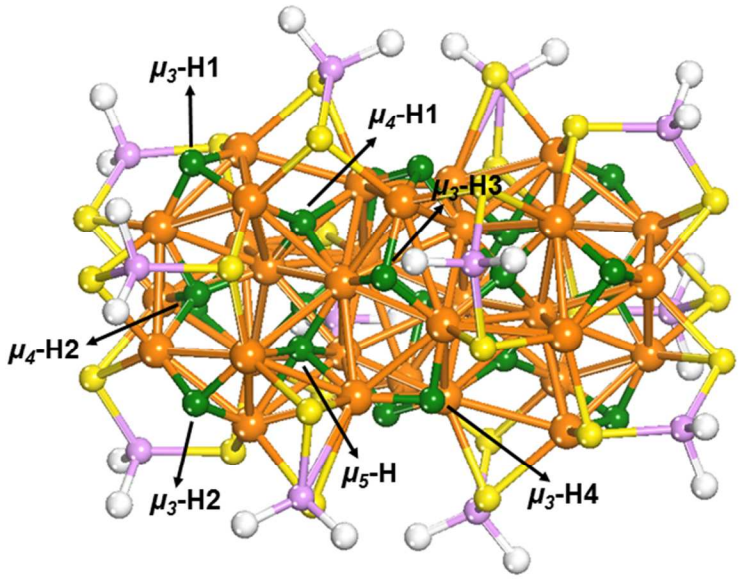

Figure 1. Atomic structure of $Cu_{32}H_{20}L_{12}$ nanocluster (L=S_2PH_2). Color code: orange, Cu; green, hydride; yellow, S; purple, P; white, H on the dithiophosphate ligands. Different types of hydrides are indicated by the arrows.

Table 1. Average Bader charges for different types and numbers of hydrides and Cu atoms in the $Cu_{32}H_{20}L_{12}$ cluster ($L=S_2PH_2$). Charge variation (minimum and maximum) are for shown in brackets.

Atom type	Number	Bader charge (|e|)
μ_3-H1	4	-0.289 [-0.294, -0.281]
μ_3-H2	2	-0.318 [-0.342, -0.293]
μ_3-H3	4	-0.267 [-0.270, -0.263]
μ_3-H4	2	-0.291 [-0.313, -0.269]
μ_4-H1	4	-0.300 [-0.317, -0.294]
μ_4-H2	2	-0.307 [-0.307, -0.307]
μ_5-H	2	-0.278 [-0.281, -0.274]
Cu (bonded to H and S)	26	+0.380 [+0.319, +0.434]
Cu (bonded to H only)	6	+0.237 [+0.210, +0.278]

3.2. CO_2 reduction to HCOOH on the $Cu_{32}H_{20}L_{12}$ nanocluster. DFT calculations showed that the exposed capping μ_3-H1 hydride has the most favorable binding for the CO_2 molecule, with a binding strength of -0.24 eV (the adsorption geometry of CO_2 is shown in Supporting Information, Figure S1). The favorable interaction is attributed to the attraction between the negatively charged hydride and the positively charged C of CO_2 reactant. After CO_2 adsorption, the next key initial step of CO_2 reduction is where the first hydrogen is added (Table 2): C or O of CO_2. If H is added to C, then the reaction will proceed to form HCOOH; if H is added to O, then the reaction will proceed to form CO.[64] We first examined the addition of H to C. Table 2 shows that there are two possible channels to form HCOO* (an intermediate adsorbed on the catalyst surface): (1) the non-electrochemical step of CO_2 reaction with one of the lattice hydrides (lattice hydride channel); (2) the electrochemical step of reacting CO_2 with the proton from solution and electron from the electrode (proton-reduction channel). Considering the many hydrides and different Cu sites in the Cu_{32} system, we exhaustively explored the HCOO* binding at different hydride and Cu sites. The relative energies are summarized in Table S3, and the structures are provided in Figures S2 (for the hydride channel) and S3 (for the proton-reduction channel). One can see that for both channels, μ_3-H1 and its associated Cu site are the most active for HCOO* binding, while the energy of HCOO* varies up to 1.25 eV

for the hydride channel and 0.76 eV for the proton-reduction channel. So in the following we focus on μ_3-H1 and its associated Cu site for CO_2 reduction.

From the computed free energy change, we found that the lattice hydride channel (Figure 2 right) is more facile, whereby the μ_3-H1 hydride in the $Cu_{32}H_{20}L_{12}$ cluster is transferred to the C atom to form adsorbed HCOO* ($Cu_{32}H_{19}L_{12}$-HCOO) with free energy of 0.32 eV. In comparison, the proton-reduction mechanism leading to formation of $Cu_{32}H_{20}L_{12}$-HCOO is highly unfavorable with a high overpotential of about 1.08 eV (Figure 2 left). In the lattice hydride channel of the HCOO* adsorption configuration (Figure S2a), the two O atoms of HCOO* are strongly bonded to the two Cu atoms on the Cu_3 triangle facet of μ_3-H1. Analysis of the electronic structure and the binding from the local density of states (LDOS) for this adsorption configuration shows that the 2*p*-orbitals of the O atom are highly hybridized with the 3*d*-orbitals of the bonded Cu atoms (Figure S7a).

Table 2. The two different channels for HCOOH and CO formation from CO_2 reduction. * represents an active site on the catalyst.

Step	Lattice hydride channel	Proton-reduction channel
HCOOH formation	$CO_2 + H^* \leftrightarrow HCOO^*$	$CO_2 + * + H^+ + e^- \leftrightarrow HCOO^*$
via 1st H addition to C	$HCOO^* + H^* \leftrightarrow HCOOH$	$HCOO^* + H^+ + e^- \leftrightarrow HCOOH$
CO formation	$CO_2 + H^* \leftrightarrow COOH^*$	$CO_2 + * + H^+ + e^- \leftrightarrow COOH^*$
via 1st H addition to O	$COOH^* + H^* \leftrightarrow CO^* + H_2O$	$COOH^* + H^+ + e^- \leftrightarrow CO^* + H_2O$

After forming the $Cu_{32}H_{19}L_{12}$-HCOO species, the second step is the addition of another hydride (μ_4-H1) to HCOO* to yield the final product, HCOOH (ΔG=0.07 eV; Figure 2 right). The loss of two lattice hydrides leads to two hydrogen vacancies in the resulting $Cu_{32}H_{18}L_{12}$ cluster, which could readily proceed via two sequential proton-reduction steps to regenerate the two reacted lattice hydrides. We found that the first hydrogen goes to the μ_3-H1 vacancy with ΔG=0.05 eV and the second goes to the μ_4-H1 vacancy with ΔG=-0.06 eV (Figure 2 right). One can see that in the more favorable lattice-hydride channel, the potential-limiting step for the HCOOH formation is the first

hydride transfer to form the HCOO* intermediate. We also considered alternative lattice-hydride mechanisms (six pathways in total; see Figure 3): for example, the first hydride addition to CO_2 is followed by a proton-reduction step instead (pathway II, III and IV in Figure 3), or the first proton-reduction step is followed by a lattice-hydride reduction step (pathway VI in Figure 3). But we found that they are less favorable than the double-hydride reduction-regeneration path (pathway I in Figure 3).

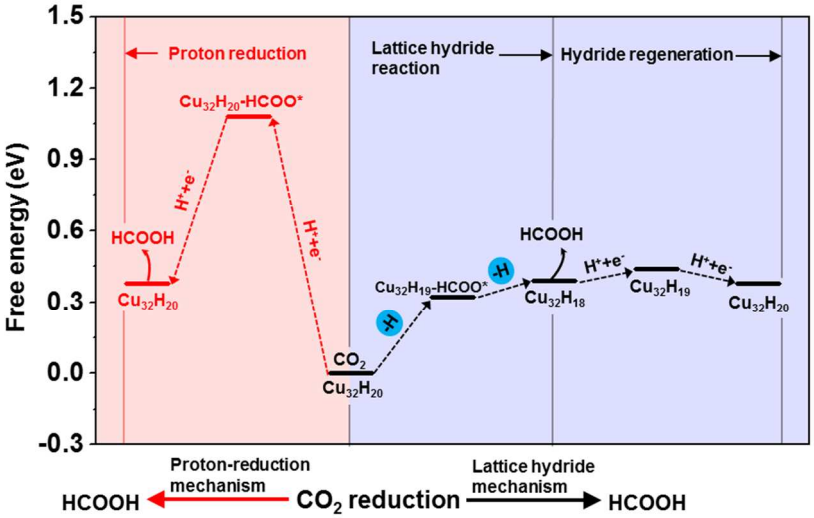

Figure 2. Reaction scheme for CO_2 electroreduction on $Cu_{32}H_{20}L_{12}$ to form HCOOH via the proton-reduction channel (to left) and the lattice-hydride channel (to right). L_{12} is omitted when labelling the intermediates.

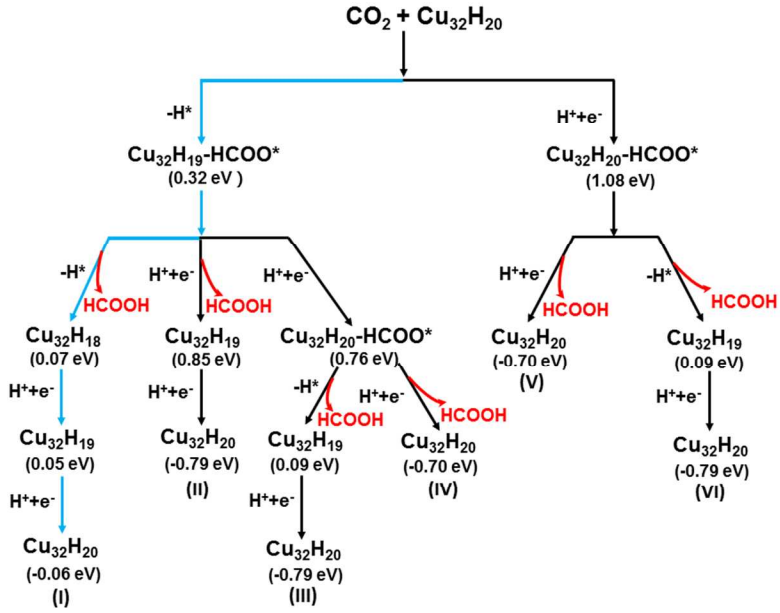

Figure 3. Reaction scheme for CO_2 electroreduction on $Cu_{32}H_{20}L_{12}$ to form HCOOH via six different pathways. The calculated free energy difference (ΔG) for each elementary step is shown under each

intermediate state. The most favorable reaction pathway is highlighted in blue, which is the same as the one in Figure 2 right. ($L=S_2PH_2$, not shown when labeling the cluster state in the scheme).

3.3. CO_2 reduction to CO on the $Cu_{32}H_{20}L_{12}$ nanocluster. CO_2 reduction to CO is another 2e-reduction process that competes with HCOOH formation and is initiated by 1st H addition to O (Table 2). We also explored the binding of COOH* and CO* intermediates at different hydrides and Cu sites (Tables S3-S4 and Figures S4-S6). Again, we found that μ_3-H1 and its associated Cu site are the most active for COOH* and CO* binding, while the energy of COOH* varies up to 0.70 eV for the hydride channel and 0.49 eV for the proton-reduction channel and the energy of CO* on the Cu site varies up to 0.30 eV. So we focus on the μ_3-H1 and its associated Cu site for mechanistic insight into CO formation. Figure 4 shows the reaction pathways for CO_2 reduction to CO on the $Cu_{32}H_{20}L_{12}$ cluster via the lattice-hydride (right) and proton-reduction (left) channels. Formation of $Cu_{32}H_{19}L_{12}$-COOH via the lattice-hydride mechanism is much more preferred (ΔG=0.81 eV) than formation of $Cu_{32}H_{20}L_{12}$-COOH via the proton-reduction channel (ΔG=1.53 eV). In the optimized structure of $Cu_{32}H_{19}L_{12}$-COOH (Figure S5a), the C atom of COOH* is bonded to two Cu atoms on the Cu_3 facet of μ_3-H1 forming tetrahedral coordination. The LDOS analysis showed strong hybridization between the 2*p*-orbital of the C atom and the 3*d*-orbitals of the bonded Cu atoms (Figure S7b). $Cu_{32}H_{19}L_{12}$-COOH is the precursor for CO-OH bond cleavage, leading to CO and OH* (ΔG= -0.43 eV). This is followed by formation of H_2O from the OH* intermediate via the lattice-hydride mechanism (ΔG=-0.16 eV). The two reacted hydrides can then be regenerated by electrochemical proton-reduction processes. Here we note that the two transferring hydrides for the CO formation are the same as those for the HCOOH formation: first, the μ_3-H1 adds to O of CO_2 to form COOH*; then, the OH* intermediate from CO-OH cleavage reacts with μ_4-H1 to form H_2O. Again, we also checked other possible reaction pathways (all the possible six pathways are shown in Figure 5), and the lattice hydride channel (pathway I in Figure 5) is the most favorable pathway for CO formation.

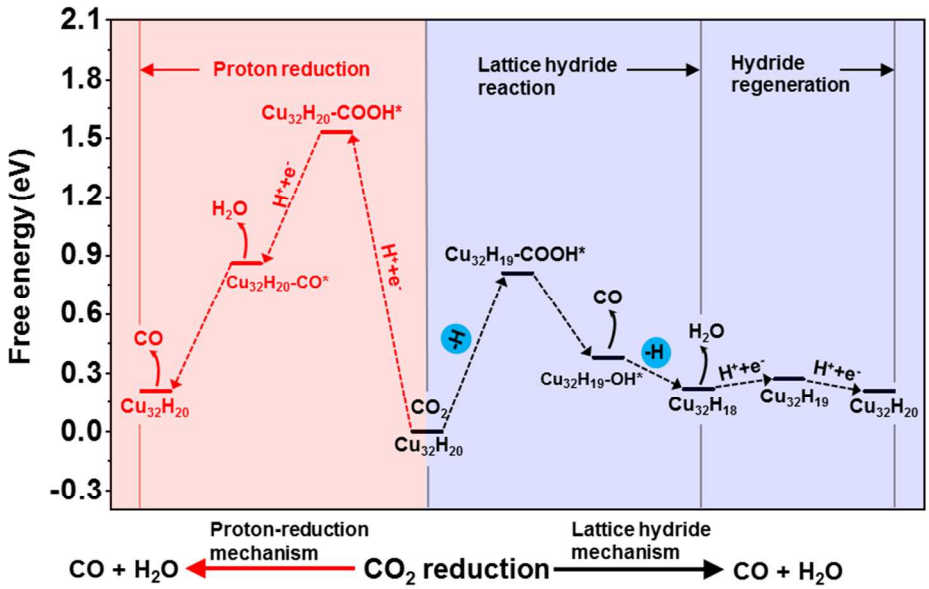

Figure 4. Reaction scheme for CO_2 electroreduction on $Cu_{32}H_{20}L_{12}$ to form CO via the proton-reduction channel (to left) and the lattice-hydride channel (to right). L_{12} is omitted when labelling the intermediates.

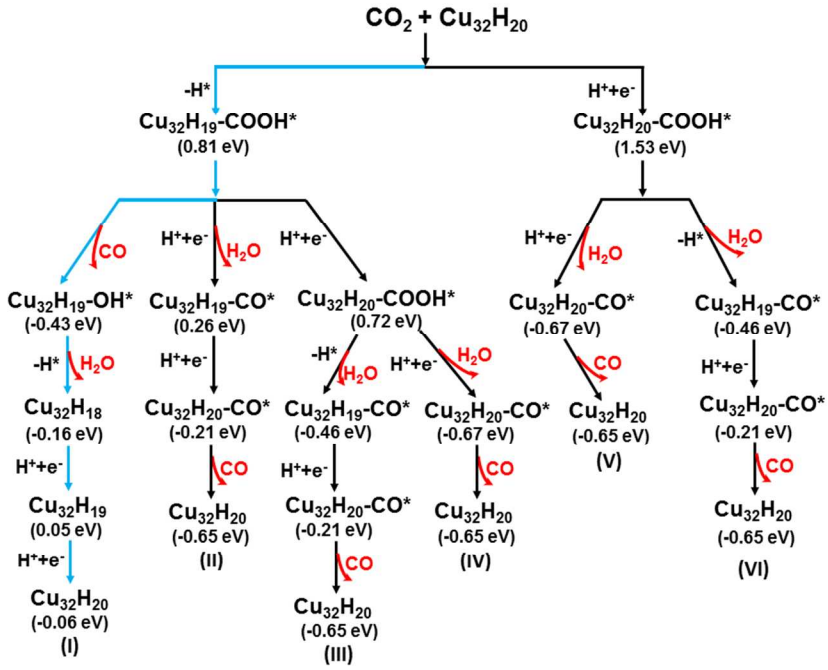

Figure 5. Reaction scheme for CO_2 electroreduction on $Cu_{32}H_{20}L_{12}$ to form CO via six different pathways. The calculated free energy difference (ΔG) for each elementary step is shown under each intermediate state. The most favorable reaction pathway (I) is highlighted in blue, which is the same as the one in Figure 4 right. ($L=S_2PH_2$, not shown when labeling the cluster state in the scheme).

Previous studies showed that the p-block dopants such as P and S atoms embedded on metal surfaces play a significant role in modulating the COOH* and CO* binding free energies because these intermediates can directly bind on the p-block dopant.[65,66] We found that the binding free energies of COOH* and CO* on the S and P sites of the -S_2PH_2 ligands are higher than on Cu (Table S4), indicating that the S and P atoms from the ligands do not play a direct role in binding the key intermediates from CO_2 reduction on the $Cu_{32}H_{20}L_{12}$ cluster

3.4. Comparison of HCOOH vs CO formation from the lattice hydride mechanism on the $Cu_{32}H_{20}L_{12}$ nanocluster. From Figures 2 and 4 one can see that both HCOOH and CO formations from CO_2 prefer the lattice-hydride mechanism on $Cu_{32}H_{20}L_{12}$. From the free-energy diagrams, the potential-determining step for both the HCOOH and CO formation derives from the first hydride transfer, with the onset potential of -0.32 V and -0.81 V vs. SHE, respectively; in other words, the overpotential is 0.32 V for HCOOH formation and 0.81 V for CO formation. Previous theoretical studies of CO_2 reduction on Cu (211) showed that the overpotential for HCOOH and CO formation is about 0.41 eV,[26] while CO formation on Cu(100) and Cu(111) needs higher overpotential (0.6 ~ 0.9 V).[28] Recent experimental reports showed that nanostructured copper electrodes can reduce the overpotential to below 0.4 V for both HCOOH and CO, compared to the polycrystalline copper electrode.[67,68] So our predicted overpotential for HCOOH is lower while that for CO is higher on $Cu_{32}H_{20}L_{12}$ than the reported ones on Cu surfaces or nanostructures.

To further shed light on the selectivity of HCOOH over CO on $Cu_{32}H_{20}L_{12}$ via the lattice-hydride mechanism, we located the transition states for the key steps leading to HCOOH and CO formations (Figure 6). One can see that the HCOOH pathway is more favorable than the CO pathway on the $Cu_{32}H_{20}L_{12}$ cluster. The key reason is that CO formation is energetically limited by formation of the COOH* intermediate (activation energy: 2.12 eV) which is much less favored than the HCOO* intermediate (activation energy: 0.89 eV). The preference of the HCOO* intermediate is due to the negatively charged lattice hydrides favoring addition to the positively charged C in CO_2, while O atoms on HCOO* are stabilized by the positively charged surface Cu atoms. This indicates that HCOOH should be the main product of CO_2 reduction on the $Cu_{32}H_{20}L_{12}$ cluster.

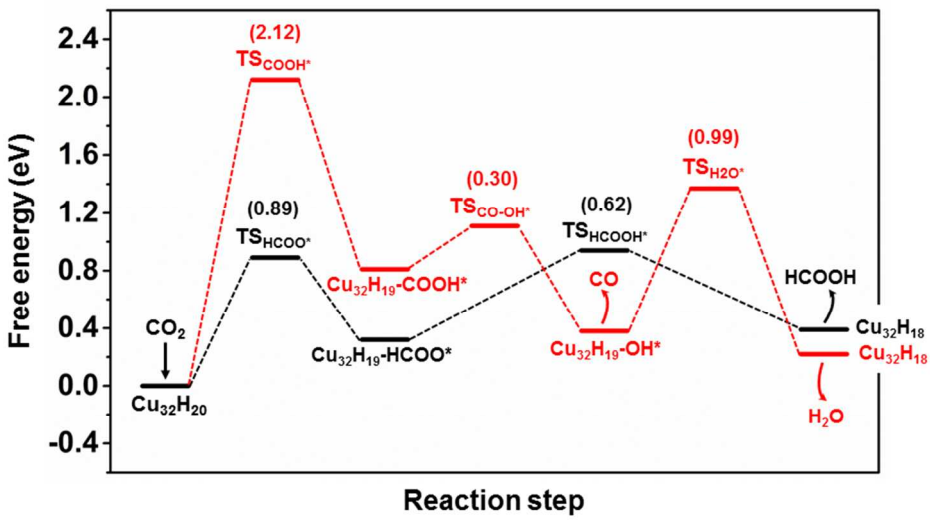

Figure 6. Free-energy diagrams for HCOOH and CO formations on the $Cu_{32}H_{20}L_{12}$ cluster via the lattice-hydride mechanism. TS = transition state. L_{12} is omitted when labelling the intermediates. The energy barriers are shown in parentheses.

HCOOH formation and the subsequent hydride regeneration on the $Cu_{32}H_{20}L_{12}$ cluster are summarized in Figure 7. For comparison, CO formation cycle is provided in Figure S8. One can clearly see that, starting from $Cu_{32}H_{20}L_{12}$ and CO_2, the μ_3-H1 hydride will first add to C to yield $Cu_{32}H_{19}L_{12}$-HCOO (Figure 7a). Notably, the two O atoms of the HCOO* intermediate are strongly bonded to the surface Cu forming a five-membered ring (Figure 7 top). The HCOO* subsequently reacts with μ_4-H1 to release the HCOOH product (Figure 7b). The resulting $Cu_{32}H_{18}L_{12}$ cluster with two hydride vacancies will then proceed through the proton-reduction processes to refill the two lattice-hydride sites (Figure 7c,d). We found that during HCOOH formation, the local structure of the Cu atoms around the two reacting hydrides did not change much, even after the loss of the interstitial μ_4-H1. This indicates that the structural stability of the Cu cluster framework can accommodate the loss of the interstitial hydrides, thereby facilitating the lattice-hydride mechanism to produce HCOOH. For comparison, CO formation is provided in Figure S8, which follows a similar cycle of the lattice-hydride mechanism.

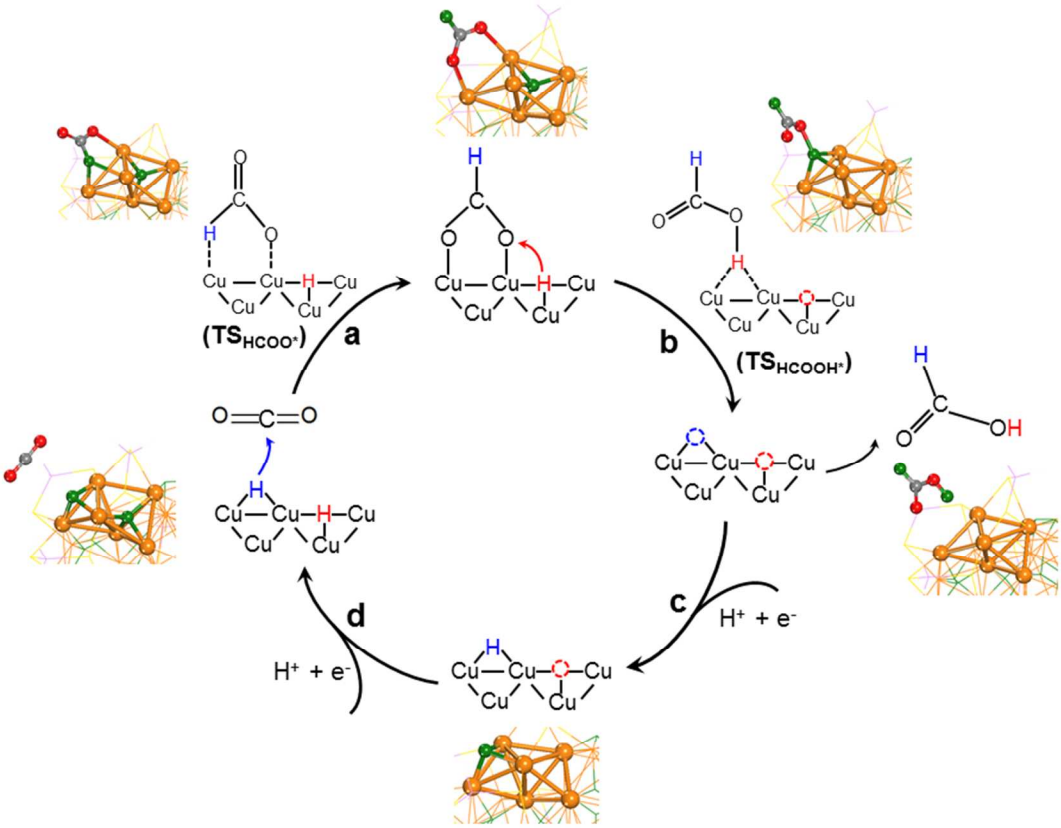

Figure 7. The overall mechanism of HCOOH formation from CO_2 reduction on $Cu_{32}H_{20}L_{12}$ via the lattice-hydride channel; the structures of the key intermediates and transition states are shown. Color code: orange, Cu; green, hydride; red, oxygen; grey, carbon; L=S_2PH_2, not shown.

3.5. Hydrogen evolution reaction (HER) on the $Cu_{32}H_{20}L_{12}$ nanocluster. HER is the major competing reaction for CO_2 electroreduction at low overpotentials, so it is necessary to compare HER vs CO_2 reduction on the $Cu_{32}H_{20}L_{12}$ nanocluster to fully evaluate its viability as an electrocatalyst for CO_2 reduction. The many hydride atoms in the $Cu_{32}H_{20}L_{12}$ nanocluster favour the Heyrovsky mechanism whereby a proton from the aqueous solution reacts with a hydride atom to generate H_2 ($Cu_{32}H_{20} + H^+ + e^- \rightarrow Cu_{32}H_{19} + H_2$). The lost hydride will be replenished by adsorbing another proton through the Volmer reaction ($Cu_{32}H_{19} + H^+ + e^- \rightarrow Cu_{32}H_{20}$). Figure 8a shows the calculated free energy for hydrogen evolution through the Heyrovsky-Volmer mechanism at different hydride sites. We can see that at lower overpotential (< 0.3 eV), the μ_4-H1, μ_4-H2 and μ_5-H will desorb from the interstitial binding sites to generate H_2, while the removal of the surface capping hydrides (μ_3-H1, μ_3-H2, μ_3-H3 and μ_3-H4) to form H_2 will require a

higher overpotential (0.6 ~ 1 eV). Figure 8b shows the kinetics for the Heyrovsky reaction at the interstitial μ_4-H1, μ_4-H2 and μ_5-H sites, and the activation barrier is 2.06 eV, 2.39 eV, and 1.58 eV, respectively. These barriers are too high to be competitive with the HCOOH formation (0.89 eV). In other words, at the low overpotential, HCOOH formation is kinetically preferred than HER. However, at high overpotentials, all these hydride channels will be open for HER.

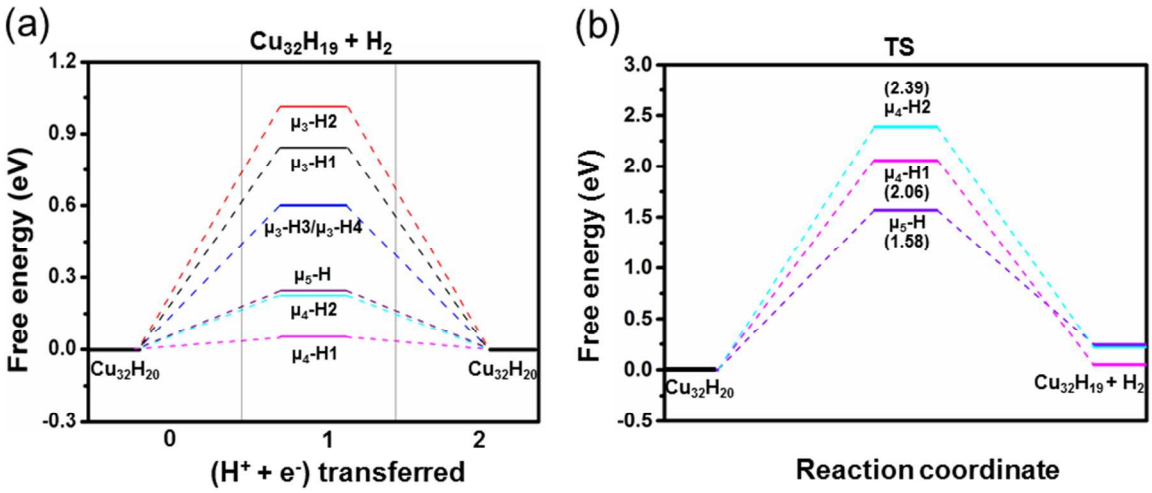

Figure 8. (a) Free energy diagram for hydrogen evolution via the Heyrovsky-Volmer mechanism ($Cu_{32}H_{20} + H^+ + e^- \rightarrow Cu_{32}H_{19} + H_2$; $Cu_{32}H_{19} + H^+ + e^- \rightarrow Cu_{32}H_{20}$) at different hydrides on $Cu_{32}H_{20}$. (b) Minimum free-energy path for the Heyrovsky reaction at the μ_4-H1, μ_4-H2 and μ_5-H sites. TS = transition state; free energy barrier heights are shown in parentheses.

3.6. Electrocatalysis experiments of CO_2 reduction on the $Cu_{32}H_{20}L_{12}$ nanocluster. To verify our theoretical prediction that CO_2 is selectively reduced to HCOOH at low overpotentials instead of to CO or losing to HER, we synthesized the $Cu_{32}H_{20}L_{12}$ nanocluster and performed controlled potential electrolysis (CPE) in 0.1 M $KHCO_3$ and 0.4 M KCl (pH 6.8) to examine its electrocatalytic activity. The as-synthesized clusters were characterized and verified to be $Cu_{32}H_{20}L_{12}$ by various techniques, including elemental analysis, ESI-MS, and ambient temperature ^{1}H and ^{31}P{^{1}H} NMR spectroscopy (Figure S9). For the electrochemical test, the $Cu_{32}H_{20}L_{12}$ clusters were first immobilized on carbon black (C) particles with Nafion that serves as a proton conductor as well as a binder.[69] The resulting particles were then dropcast on a GDL to form a composite Cu_{32}/C/GDL electrode.

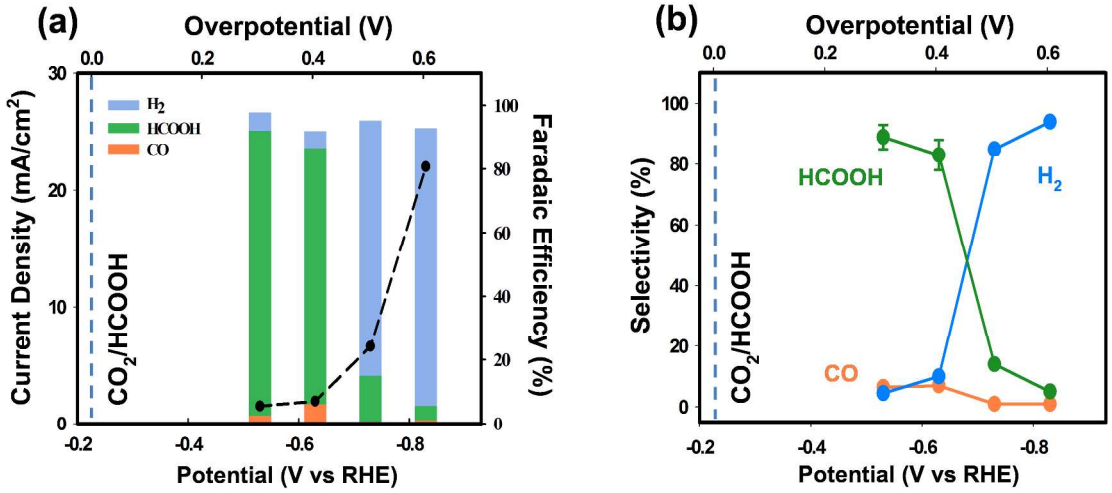

Figure 9. (a) Average current densities (black circles) and cumulative faradaic efficiencies for H_2, HCOOH, and CO (stacked bars) obtained at different overpotentials. (b) Product selectivity for H_2, HCOOH, and CO produced at different overpotentials. Controlled potential electrolysis (CPE) was conducted for 90 min in 0.1 M $KHCO_3$ and 0.4 M KCl (pH 6.8) on a Cu_{32}/C/GDL electrode (1 cm^2).

Figure 9 shows the results of CO_2 electroreduction on the $Cu_{32}H_{20}L_{12}$ nanocluster. As can be seen from Figure 9a, the average current density during 90 min CPE becomes significant at the overpotential of 0.3 V and increases with overpotential. Figure 9a also shows the cumulative Faradaic efficiency of the product formation after 90 min CPE at different overpotentials: H_2, HCOOH, and CO were detected as the main products accounting for the cumulative Faradaic efficiency of >90%. The selectivity of these three products is compared as a function of overpotential in Figure 9b. One can see that the $Cu_{32}H_{20}L_{12}$ nanocluster predominantly produces HCOOH (as $HCOO^-$ at pH 6.8) at low overpotentials (89% at 0.3 V and 83% at 0.4 V), with minor amounts of CO and H_2. By contrast, the product selectivity dramatically changes when the overpotential is higher than 0.5 V where H_2 is predominantly produced (85% at 0.5 V and 94% at 0.6 V). These experimental results are in excellent agreement with our DFT prediction that HCOOH formation is favored at low overpotential, while HER dominates at higher overpotential. The $Cu_{32}H_{20}L_{12}$ nanocluster is quite stable during electrocatalysis at pH 6.8: the Faradaic efficiency of HCOOH (and H_2 and CO) formation monitored at different CPE time (at the overpotential of 0.3 V) was found to be unchanged during the first 90 min and slightly

decreased at 180 min (Figure S10). We further analyzed the turnover number of the $Cu_{32}H_{20}L_{12}$ cluster for HCOOH production and found it to be 1740 moles of HCOOH per mole of $Cu_{32}H_{20}L_{12}$ after 90 min CPE, supporting the replenishment of the lattice hydrides during the CO_2 reduction. For comparison, Cu(0) nanoparticles produced mainly CO at low overpotentials,[67] while Cu foil produced mainly H_2 at low overpotentials.[8]

3.7. Implications of the lattice hydride mechanism. So far we have shown that the key steps and product selectivity of electroreduction of CO_2 on a typical atomically precise copper-hydride cluster. The vast majority of previous work of electroreduction of CO_2 on Cu has focused on flat surfaces and large Cu nanoparticles. It has been found that on the pure Cu surface, HCOOH and CO formations are competitive in the initial electrochemical step of CO_2 reduction but CO is the major product.[13] Very recent theoretical studies of CO_2 reduction on Cu(100)[70] found that $HCOO^-$ formation needs to overcome a higher free energy barrier (0.80 eV) than CO formation (0.43 eV). By contrast, on the $Cu_{32}H_{20}L_{12}$ cluster examined here, the presence of the negatively charged hydride facilitates the formation of HCOO* intermediate, favoring formation of HCOOH instead of CO. So the structurally precise Cu-hydride clusters offer distinctly different pathways and product selectivity. Moreover, to the best of our knowledge, our work is the first time that the lattice-hydride mechanism has been proposed for electrochemical CO_2 reduction on a heterogeneous or nanocluster catalyst.

We have now demonstrated electroreduction of CO_2 in aqueous 0.1 M $KHCO_3$ on the copper-hydride clusters. This electrolyte has also been used in electroreduction of CO_2 to CO on the Au_{25} nanocluster previously.[71] In the future, we think that it will be also worthwhile to use non-aqueous electrolytes such as organic solvents or ionic liquids for CO_2 reduction on the copper-hydride clusters. As demonstrated experimentally, these non-aqueous electrolytes can supply protons in two ways: (1) by mixing a low concentration (~100 ppm) of water in the organic or ionic liquid electrolyte;[72] (2) by using a protic solvent such as methanol.[73] In addition, the lattice-hydride mechanism of CO_2 reduction can be a general pathway beyond the Cu clusters, given the recent success in synthesizing other hydride-containing transition-metal clusters.[74,75]

4. CONCLUSIONS

In summary, we have demonstrated that structurally precise copper-hydride nanoclusters offer unique product selectivity for electroreduction of CO_2 at low overpotentials. Based on a prototypical such cluster, $Cu_{32}H_{20}L_{12}$, we predicted from density functional theory that both the hydride ligands and the surface Cu play a critical role in promoting the reduction process, leading to HCOOH instead of CO at low overpotentials; more important, CO_2 reduction was also predicted to be kinetically preferred than hydrogen evolution. We found that HCOOH formation proceeds through two steps of lattice-hydride reduction: CO_2 reacts directly with the capping hydride to form HCOO* which then reacts with another interstitial hydride to form HCOOH. The reacted hydrides can be regenerated facilely by proton reduction. The predictions were confirmed by our electrochemical testing of CO_2 reduction on the synthesized $Cu_{32}H_{20}L_{12}$ cluster: $HCOO^-$ was found to be the main product (> 80% selectivity), with minor amounts of CO and H_2, at low overpotentials with a Faradaic efficiency over 90% with a turnover number of 1740 for the first 90 min. Our work hence paves the way for the use of the structurally precise copper-hydride nanoclusters to explore the electrocatalytic CO_2 reduction. The lattice-hydride mechanism can be a general path on hydride-containing transition-metal nanoclusters and hence may offer unique product selectivity than traditional electrocatalysts for CO_2 reduction.

ACKNOWLEDGEMENTS

This work was supported by the University of California, Riverside. This research used resources of the National Energy Research Scientific Computing Center, a DOE Office of Science User Facility supported by the Office of Science of the U.S. Department of Energy under Contract DE-AC02-05CH11231. D.L. acknowledges support from the Korea CCS R&D Center (KCRC) grant (NRF-2014M1A8A1074219) and the NRF grants (NRF-2014R1A2A1A11051032 and 2009-0093823). C. W. Liu acknowledges support from the Ministry of Science and Technology in Taiwan (MOST 103-2113-M-259-003).

Supporting Information Available:

- Details of corrections in terms of free-energy profiles.
- Adsorption sites, electronic structure, geometry, and energetics of key intermediates.
- Scheme of CO production cycle.
- Synthesis details and characterization data.
- Faradaic efficiency formation monitored at different times at a fixed overpotential.

REFERENCES

(1) Davis, S. J.; Caldeira, K.; Matthews, H. D. *Science* **2010**, *329*, 1330-1333.

(2) Parrenin, F.; Masson-Delmotte, V.; Kohler, P.; Raynaud, D.; Paillard, D.; Schwander, J.; Barbante, C.; Landais, A.; Wegner, A.; Jouzel, J. *Science* **2013**, *339*, 1060-1063.

(3) Olah, G. A.; Prakash, G. K. S.; Goeppert, A. *J. Am. Chem. Soc.* **2011**, *133*, 12881-12898.

(4) Song, C. S. *Catal. Today* **2006**, *115*, 2-32.

(5) Whipple, D. T.; Kenis, P. J. A. *J. Phys. Chem. Lett.* **2010**, *1*, 3451-3458.

(6) Benson, E. E.; Kubiak, C. P.; Sathrum, A. J.; Smieja, J. M. *Chem. Soc. Rev.* **2009**, *38*, 89-99.

(7) Hori, Y. In *Modern Aspects of Electrochemistry, No 42*; Springer, New York: 2008, p 89-189.

(8) Hori, Y.; Murata, A.; Takahashi, R. *J. Chem. Soc., Faraday Trans. I* **1989**, *85*, 2309-2326.

(9) Hori, Y.; Kikuchi, K.; Suzuki, S. *Chem. Lett.* **1985**, 1695-1698.

(10) Gattrell, M.; Gupta, N.; Co, A. *J. Electroanal. Chem.* **2006**, *594*, 1-19.

(11) Hori, Y.; Takahashi, R.; Yoshinami, Y.; Murata, A. *J. Phys. Chem. B* **1997**, *101*, 7075-7081.

(12) Hori, Y.; Kikuchi, K.; Murata, A.; Suzuki, S. *Chem. Lett.* **1986**, 897-898.

(13) Hori, Y.; Murata, A.; Takahashi, R.; Suzuki, S. *J. Am. Chem. Soc.* **1987**, *109*, 5022-5023.

(14) Kuhl, K. P.; Cave, E. R.; Abram, D. N.; Jaramillo, T. F. *Energy Environ. Sci.* **2012**, *5*, 7050-7059.

(15) Kuhl, K. P.; Hatsukade, T.; Cave, E. R.; Abram, D. N.; Kibsgaard, J.; Jaramillo, T. F. *J. Am. Chem. Soc.* **2014**, *136*, 14107-14113.

(16) Hori, Y.; Takahashi, I.; Koga, O.; Hoshi, N. *J. Phys. Chem. B* **2002**, *106*, 15-17.

(17) Schouten, K. J. P.; Kwon, Y.; van der Ham, C. J. M.; Qin, Z.; Koper, M. T. M. *Chem. Sci.* **2011**, *2*, 1902-1909.

(18) Schouten, K. J. P.; Qin, Z. S.; Gallent, E. P.; Koper, M. T. M. *J. Am. Chem. Soc.* **2012**, *134*, 9864-9867.

(19) Cook, R. L.; Macduff, R. C.; Sammells, A. F. *J. Electrochem. Soc.* **1989**, *136*, 1982-1984.

(20) Raciti, D.; Livi, K. J.; Wang, C. *Nano Lett.* **2015**, *15*, 6829-6835.

(21) Loiudice, A.; Lobaccaro, P.; Kamali, E. A.; Thao, T.; Huang, B. H.; Ager, J. W.; Buonsanti, R. *Angew. Chem. Int. Ed.* **2016**, *55*, 5789-5792.

(22) Yang, K. D.; Ko, W. R.; Lee, J. H.; Kim, S. J.; Lee, H.; Lee, M. H.; Nam, K. T. *Angew. Chem. Int. Ed.* **2017**, *56*, 796-800.

(23) Huang, Y.; Handoko, A. D.; Hirunsit, P.; Yeo, B. S. *ACS Catal.* **2017**, *7*, 1749-1756.

(24) Ma, S.; Sadakiyo, M.; Heima, M.; Luo, R.; Haasch, R. T.; Gold, J. I.; Yamauchi, M.; Kenis, P. J. A. *J. Am. Chem. Soc.* **2017**, *139*, 47-50.

(25) Huan, T. N.; Simon, P.; Rousse, G.; Genois, I.; Artero, V.; Fontecave, M. *Chem. Sci.* **2017**, *8*, 742-747.

(26) Peterson, A. A.; Abild-Pedersen, F.; Studt, F.; Rossmeisl, J.; Norskov, J. K. *Energy Environ. Sci.* **2010**, *3*, 1311-1315.

(27) Nie, X. W.; Esopi, M. R.; Janik, M. J.; Asthagiri, A. *Angew. Chem. Int. Ed.* **2013**, *52*, 2459-2462.

(28) Durand, W. J.; Peterson, A. A.; Studt, F.; Abild-Pedersen, F.; Norskov, J. K. *Surf. Sci.* **2011**, *605*, 1354-1359.

(29) Peterson, A. A.; Norskov, J. K. *J. Phys. Chem. Lett.* **2012**, *3*, 251-258.

(30) Calle-Vallejo, F.; Koper, M. T. M. *Angew. Chem. Int. Ed.* **2013**, *52*, 7282-7285.

(31) Xiao, H.; Cheng, T.; Goddard, W. A.; Sundararaman, R. *J. Am. Chem. Soc.* **2016**, *138*, 483-486.

(32) Montoya, J. H.; Shi, C.; Chan, K.; Norskov, J. K. *J. Phys. Chem. Lett.* **2015**, *6*, 2032-2037.

(33) Manthiram, K.; Beberwyck, B. J.; Aivisatos, A. P. *J. Am. Chem. Soc.* **2014**, *136*, 13319-13325.

(34) Reske, R.; Mistry, H.; Behafarid, F.; Cuenya, B. R.; Strasser, P. *J. Am. Chem. Soc.* **2014**, *136*, 6978-6986.

(35) Baturina, O. A.; Lu, Q.; Padilla, M. A.; Xin, L.; Li, W. Z.; Serov, A.; Artyushkova, K.; Atanassov, P.; Xu, F.; Epshteyn, A.; Brintlinger, T.; Schuette, M.; Collins, G. E. *ACS Catal.* **2014**, *4*, 3682-3695.

(36) Jin, R. C. *Nanoscale* **2015**, *7*, 1549-1565.

(37) Jin, R.; Zeng, C.; Zhou, M.; Chen, Y. *Chem. Rev.* **2016**, *116*, 10346-10413.

(38) Joshi, C. P.; Bootharaju, M. S.; Bakr, O. M. *J. Phys. Chem. Lett.* **2015**, *6*, 3023-3035.

(39) Desireddy, A.; Conn, B. E.; Guo, J. S.; Yoon, B.; Barnett, R. N.; Monahan, B. M.; Kirschbaum, K.; Griffith, W. P.; Whetten, R. L.; Landman, U.; Bigioni, T. P. *Nature* **2013**, *501*, 399-402.

(40) Dhayal, R. S.; Liao, J.-H.; Liu, Y.-C.; Chiang, M.-H.; Kahlal, S.; Saillard, J.-Y.; Liu, C. W. *Angew. Chem. Int. Ed.* **2015**, *54*, 3702-3706.

(41) Dhayal, R. S.; Lin, Y.-R.; Liao, J.-H.; Chen, Y.-J.; Liu, Y.-C.; Chiang, M.-H.; Kahlal, S.; Saillard, J.-Y.; Liu, C. W. *Chem. Eur.J* **2016**, *22*, 9943-9947.

(42) Yang, H.; Wang, Y.; Huang, H.; Gell, L.; Lehtovaara, L.; Malola, S.; Häkkinen, H.; Zheng, N. *Nat. Commun.* **2013**, *4*, 2422.

(43) Jadzinsky, P. D.; Calero, G.; Ackerson, C. J.; Bushnell, D. A.; Kornberg, R. D. *Science* **2007**, *318*, 430-433.

(44) Heaven, M. W.; Dass, A.; White, P. S.; Holt, K. M.; Murray, R. W. *J. Am. Chem. Soc.* **2008**, *130*, 3754-3755.

(45) McKenzie, L. C.; Zaikova, T. O.; Hutchison, J. E. *J. Am. Chem. Soc.* **2014**, *136*, 13426-13435.

(46) Maity, P.; Tsunoyama, H.; Yamauchi, M.; Xie, S. H.; Tsukuda, T. *J. Am. Chem. Soc.* **2011**, *133*, 20123-20125.

(47) Wan, X.-K.; Tang, Q.; Yuan, S.-F.; Jiang, D.-E.; Wang, Q.-M. *J. Am. Chem. Soc.* **2015**, *137*, 652-655.

(48) Wan, X.-K.; Yuan, S.-F.; Tang, Q.; Jiang, D.-E.; Wang, Q.-M. *Angew. Chem. Int. Ed.* **2015**, *54*, 5977-5980.

(49) Wan, X.-K.; Xu, W. W.; Yuan, S.-F.; Gao, Y.; Zeng, X.-C.; Wang, Q.-M. *Angew. Chem., Int. Ed.*. **2015**, *127*, 9683-9686.

(50) Dhayal, R. S.; van Zyl, W. E.; Liu, C. W. *Acc. Chem. Res.* **2016**, *49*, 86-95.

(51) Nguyen, T.-A. D.; Goldsmith, B. R.; Zaman, H. T.; Wu, G.; Peters, B.; Hayton, T. W. *Chem. Eur. J.* **2015**, *21*, 5341-5344.

(52) Huertos, M. A.; Cano, I.; Bandeira, N. A. G.; Benet-Buchholz, J.; Bo, C.; van Leeuwen, P. *Chem. Eur. J.* **2014**, *20*, 16121-16127.

(53) Dhayal, R. S.; Liao, J. H.; Wang, X. P.; Liu, Y. C.; Chiang, M. H.; Kahlal, S.; Saillard, J. Y.; Liu, C. W. *Angew. Chem. Int. Ed.* **2015**, *54*, 13604-13608.

(54) Dhayal, R. S.; Liao, J.-H.; Lin, Y.-R.; Liao, P.-K.; Kahlal, S.; Saillard, J.-Y.; Liu, C. W. *J. Am. Chem. Soc.* **2013**, *135*, 4704-4707.

(55) Nguyen, T.-A. D.; Jones, Z. R.; Goldsmith, B. R.; Buratto, W. R.; Wu, G.; Scott, S. L.; Hayton, T. W. *J. Am. Chem. Soc.* **2015**, *137*, 13319-13324.

(56) Edwards, A. J.; Dhayal, R. S.; Liao, P. K.; Liao, J. H.; Chiang, M. H.; Piltz, R. O.; Kahlal, S.; Saillard, J. Y.; Liu, C. W. *Angew. Chem. Int. Ed.* **2014**, *53*, 7214-7218.

(57) Dhayal, R. S.; Liao, J.-H.; Kahlal, S.; Wang, X.; Liu, Y.-C.; Chiang, M.-H.; van Zyl, W. E.; Saillard, J.-Y.; Liu, C. W. *Chem. Eur. J.* **2015**, *21*, 8369-8374.

(58) Kresse, G.; Furthmuller, J. *Phys. Rev. B* **1996**, *54*, 11169-11186.

(59) Blochl, P. E. *Phys. Rev. B* **1994**, *50*, 17953-17979.

(60) Perdew, J. P.; Burke, K.; Ernzerhof, M. *Phys. Rev. Lett.* **1996**, *77*, 3865-3868.

(61) Grimme, S.; Antony, J.; Ehrlich, S.; Krieg, H. *J. Chem. Phys.* **2010**, *132*, 154104.

(62) Henkelman, G.; Uberuaga, B. P.; Jonsson, H. *J. Chem. Phys.* **2000**, *113*, 9901-9904.

(63) Nørskov, J. K.; Rossmeisl, J.; Logadottir, A.; Lindqvist, L.; Kitchin, J. R.; Bligaard, T.; Jónsson, H. *J. Phys. Chem. B* **2004**, *108*, 17886-17892.

(64) Kortlever, R.; Shen, J.; Schouten, K. J. P.; Calle-Vallejo, F.; Koper, M. T. M. *J. Phys. Chem. Lett.* **2015**, *6*, 4073-4082.

(65) Lim, H.-K.; Shin, H.; Goddard, W. A.; Hwang, Y. J.; Min, B. K.; Kim, H. *J. Am. Chem. Soc.* **2014**, *136*, 11355-11361.

(66) Shin, H.; Ha, Y.; Kim, H. *J. Phys. Chem. Lett.* **2016**, *7*, 4124-4129.

(67) Li, C. W.; Kanan, M. W. *J. Am. Chem. Soc.* **2012**, *134*, 7231-7234.

(68) Qiao, J. L.; Jiang, P.; Liu, J. S.; Zhang, J. J. *Electrochem. Commun.* **2014**, *38*, 8-11.

(69) Kwak, K.; Choi, W.; Tang, Q.; Kim, M.; Lee, Y.; Jiang, D. E.; Lee, D. *Nat. Commun.* **2017**, *8*, 14723.

(70) Cheng, T.; Xiao, H.; Goddard, W. A. *J. Am. Chem. Soc.* **2016**, *138*, 13802-13805.

(71) Kauffman, D. R.; Alfonso, D.; Matranga, C.; Qian, H.; Jin, R. *J. Am. Chem. Soc.* **2012**, *134*, 10237-10243.

(72) Asadi, M.; Kim, K.; Liu, C.; Addepalli, A. V.; Abbasi, P.; Yasaei, P.; Phillips, P.; Behranginia, A.; Cerrato, J. M.; Haasch, R.; Zapol, P.; Kumar, B.; Klie, R. F.; Abiade, J.; Curtiss, L. A.; Salehi-Khojin, A. *Science* **2016**, *353*, 467-470.

(73) Murugananthan, M.; Kaneco, S.; Katsumata, H.; Suzuki, T.; Kumaravel, M. In *Green Carbon Dioxide*; John Wiley & Sons, Inc.: 2014, p 191-214.

(74) Bootharaju, M. S.; Dey, R.; Gevers, L. E.; Hedhili, M. N.; Basset, J. M.; Bakr, O. M. *J. Am. Chem. Soc.* **2016**, *138*, 13770-13773.

(75) Ohki, Y.; Shimizu, Y.; Araake, R.; Tada, M.; Sameera, W. M. C.; Ito, J.-I.; Nishiyama, H. *Angew.Chem. Int.Ed.* **2016**, *55*, 15821-15825.

TOC GRAPHIC